Chemical Engineering Journal 535 (2026) 175471

Contents lists available at ScienceDirect

Chemical Engineering Journal

journal homepage: www.elsevier.com/locate/cej

Spatially engineered polymer-in-salt electrolytes for solid-state lithium–sulfur batteries

Haeli Lee [a], Nagyeong Shin [a], Taehyun Kim [a], Minho Jung [a], Seung Gi Jung [a], Jinhan Cho [a], Holger Althues [b], Jun Hyuk Moon [a,*]

[a] *Department of Chemical and Biological Engineering, Korea University, 145 Anam-ro, Seongbuk-gu, Seoul, 02841, Republic of Korea*
[b] *Fraunhofer Institute for Material and Beam Technology IWS, Winterbergstrasse 28, Dresden, 01277, Germany*

ARTICLE INFO

Keywords:
Polymer-in-salt electrolyte
Solid-state lithium–sulfur battery
Asymmetric electrolyte architecture
Polysulfide suppression
Lithium metal anode
Sustainable energy storage

ABSTRACT

Solid-state electrolytes (SSEs) suppress polysulfide shuttling in lithium–sulfur (Li—S) batteries yet introduce intrinsic barriers by slowing solid-state sulfur conversion. Here, we introduce an asymmetric, region-specific polymer-in-salt (PIS) electrolyte architecture that addresses these coupled limitations. The poly(vinylidene fluoride-*co*-hexafluoropropylene) (PVDF-HFP) PIS matrix suppresses polysulfide crossover and provides an ionic conductivity of 5.3×10^{-4} S cm^{-1}; a polyethylene oxide (PEO)–rich cathode interface enables stepwise sulfur conversion mediated by lithium polysulfides; and a lithium aluminum titanium phosphate (LATP)–reinforced anode-side electrolyte increases the Li^+ transference number to 0.59 while maintaining stable Li-metal cycling for more than 350 h. Li—S cells using this architecture deliver an initial capacity of 1180 mAh g^{-1} at 0.05C (1 mg S cm^{-2}) and retain 78% of their capacity after 120 cycles at 0.2C. At a sulfur loading of 2.7 mg cm^{-2} and an N/P ratio of 4.5, the cells retain 80% of their capacity over 50 cycles. These results demonstrate that spatially decoupling electrolyte functions at the cathode, bulk, and anode interfaces provides a scalable and mechanistically grounded design principle for improved solid-state Li—S batteries.

1. Introduction

Lithium–sulfur (Li—S) batteries are widely recognized as a promising next-generation energy storage technology due to their high theoretical capacity (1675 mAh g^{-1}) and energy density (2600 Wh kg^{-1}), which exceed those of conventional lithium-ion batteries (LIBs). [1–4] However, their practical deployment is limited by intrinsic challenges, particularly the dissolution and uncontrolled migration of lithium polysulfides (LiPS) in liquid electrolytes. [5,6] These processes lead to active material loss, the shuttle effect, and rapid capacity fading, thereby undermining long-term cycling stability. [7,8]

Solid-state electrolytes (SSEs) have been explored as attractive alternatives because their intrinsically low LiPS solubility suppresses shuttle effects and offers the potential for stable cycling. [9,10] Both inorganic SSEs (e.g., sulfide-based $Li_{10}GeP_2S_{12}$, Li_6PS_5Cl and oxide-based $Li_7La_3Zr_2O_{12}$, $Li_{1+x}Al_xTi_{2-x}(PO_4)_3$) and polymer-based SSEs (e.g., polyethylene oxide (PEO), polymethyl methacrylate (PMMA), and polyvinylidene fluoride (PVDF-HFP) systems) have been investigated, along with hybrid or quasi-solid configurations that integrate SSEs selectively at one electrode. [11–15] For example, sulfide-based systems have delivered discharge capacities up to ~1210 mAh g^{-1} under moderate rates at elevated temperatures, while poly(dioxolane)-based quasi-solid cells with engineered interphases have sustained ~75% capacity retention over 100 cycles. [16–18]

Yet these advances expose a critical trade-off. Suppressing LiPS solubility removes the shuttle problem but also eliminates LiPS-mediated pathways; sulfur conversion must therefore proceed through solid–solid reactions with intrinsically slow kinetics. [19,20] At the same time, interfacial contact at the lithium-metal anode is often incomplete, leading to void formation, increased charge-transfer resistance, and accelerated dendrite initiation. [21] As a result, sulfide-based SSE cells frequently deliver less than ~850 mAh g^{-1} at 0.2C, with further deterioration at higher currents, [22] and the moisture sensitivity and high precursor costs of sulfide electrolytes pose further scalability challenges. [23,24] Meanwhile polymer electrolytes under high sulfur loading—conditions where sluggish kinetics become most severe—have been rarely reported. Thus, the adoption of SSEs amplifies distinct interfacial challenges at both the sulfur cathode and lithium-metal

---

* Corresponding author.
E-mail address: junhyukmoon@korea.ac.kr (J.H. Moon).

https://doi.org/10.1016/j.cej.2026.175471
Received 23 December 2025; Received in revised form 14 February 2026; Accepted 21 March 2026
Available online 24 March 2026

anode, highlighting the need for electrolyte architectures capable of simultaneously regulating these opposing issues.

Here we present a polymer-based all-solid-state electrolyte with a region-specific architecture to address these challenges. A PVDF-HFP polymer-in-salt (PIS) matrix serves as the bulk electrolyte and provides a high-conductivity ion transport pathway; a PEO-based PIS interlayer at the cathode restores LiPS-mediated reaction pathways and enables stepwise sulfur conversion; and a nanofiller-reinforced PVDF-HFP layer at the anode maintains intimate contact with lithium metal while providing mechanical stability to suppress void formation and dendrite initiation. This asymmetric configuration integrates the stability of solid-state electrolytes with the kinetic advantages of LiPS-mediated chemistry (Fig. 1). Under sulfur loadings of 1–3 mg cm^{-2} and an N/P ratio of 4.5, cells using this architecture deliver 1180 mAh g^{-1} and retain 80% of their initial capacity after 50 cycles. This region-specific electrolyte design therefore provides a scalable route to overcoming the long-standing trade-offs in SSE-based Li—S batteries.

2. Results and discussion

PIS electrolytes contain a lithium salt fraction exceeding 50 wt% of the total polymer–salt composition, [25,26] substantially higher than conventional salt-in-polymer (SIP) systems. This high salt content promotes ion migration through extended cluster networks rather than polymer segmental motion, resulting in substantially higher lithium-ion diffusivity. [27] We prepared PIS by mixing lithium bis(trifluoromethanesulfonyl)imide (LiTFSI) with a PVDF-HFP matrix in a fixed mass ratio of 1:1. PVDF-HFP was selected because its hydrophobic C—F bonds exhibit low affinity toward LiPS and facilitate ion clustering even at low polymer content. [17] For comparison, a conventional salt-in-polymer (SIP) electrolyte was prepared by incorporating 20 wt% LiTFSI into PVDF-HFP (Fig. S1). [28]

Morphological analysis revealed that PIS exhibited higher porosity than SIP, attributable to microphase separation induced by the high salt content (Fig. 2a and Fig. S2). EDS mapping showed sulfur signals from LiTFSI clustered near pores in PIS, indicating locally aggregated salt-rich domains (Fig. 2b). Differential scanning calorimetry (DSC) further supported this phase-separated structure, with PIS exhibiting a substantially lower glass transition temperature (T_g) than PVDF-HFP or SIP (Fig. S3). [29] Mechanical testing showed that the tensile strength of PIS was 1.11 MPa, corresponding to 21% of that of SIP (Fig. 2c). The reduction in strength is attributed to stress concentrations at the boundaries of the microphase-separated domains. The coordination environment of PIS was analyzed by Raman spectroscopy. A characteristic band at ~740–750 cm^{-1}, assigned to the symmetric N—S stretching of TFSI$^-$, was deconvoluted into three coordination states: free anions (~740 cm^{-1}), contact ion pairs (CIP, ~744 cm^{-1}), and aggregated clusters (AGG, ~749 cm^{-1}) (Fig. 2d and Fig. S4). [25,30,31] SIP contained a larger fraction of free TFSI$^-$, whereas PIS contained a higher proportion of AGG, indicating enhanced ion clustering. [32]

Bulk ion transport in PIS was analyzed by electrochemical impedance spectroscopy (EIS). A 20 μm-thick PIS film exhibited an ionic conductivity of 5.3×10^{-4} S cm^{-1}, nearly an order of magnitude higher than that of SIP films (Fig. 2e). Temperature-dependent measurements yielded activation energies of 0.11 eV for PIS and 0.23 eV for SIP (Fig. S5), confirming that Li$^+$ migration in PIS proceeds with a substantially lower energy barrier than in SIP. These results are consistent with the coordination environments identified by Raman spectroscopy, suggesting that aggregated ion clusters suppress anion mobility and thereby enhance Li$^+$ transport. [33] The lithium-ion transference number (t_+)—defined as the fraction of current carried by Li$^+$ under steady-state conditions—was determined using the Bruce–Vincent method, which combines potentiostatic polarization with impedance measurements before and after polarization. [34] PIS exhibited a t_+ of 0.57, substantially higher than the 0.36 measured for SIP (Fig. 2f), indicating restricted TFSI$^-$ mobility and an enhanced contribution of Li$^+$ to overall ion transport.

The electrochemical performance of PIS was further evaluated in symmetric Li|Li cells under galvanostatic cycling. The PIS cell operated stably for more than 300 h without short-circuiting, while maintaining a lower polarization voltage throughout cycling, reflecting lower internal resistance and suppressed concentration polarization compared with SIP, which failed after 79 h (Fig. 2g). [35,36] Critical current density (CCD) measurements further showed that PIS supported current densities up to 2.8 mA cm^{-2} without short-circuiting, compared to ~0.4 mA cm^{-2} for SIP (Fig. 2h and Fig. S6). This higher CCD resulted from the high ionic conductivity and elevated Li$^+$ transference number of the PIS electrolyte. [37]

PIS electrolytes exhibit minimal LiPS solubility; however, this constraint enforces a direct solid-state conversion pathway, which is known to limit sulfur redox kinetics. [38,39] Sulfur cathodes in PIS environments often display elevated overpotentials and sluggish charge–discharge profiles, indicative of kinetic barriers. [40,41] To address this issue, we constructed a sulfur cathode with a PEO-based interfacial layer capable of dissolving LiPS. A thin PEO-containing polymer coating was first applied to the sulfur cathode surface, as shown in Fig. 3a (before coating) and Fig. 3b (after coating), followed by the infiltration of PVDF-HFP–based PIS to fill the remaining porous structure (Fig. 3c). FT-IR analysis of the dried PEO and PIS films showed that solvent-related peaks were no longer observed, indicating that residual solvent is negligible (Fig. S7). The PEO-rich layer enables LiPS-mediated conversion, while the outer PIS layer suppresses LiPS diffusion and forms a chemically compatible interface with the bulk PIS electrolyte. Sequential casting of the two polymer layers showed no visible delamination or

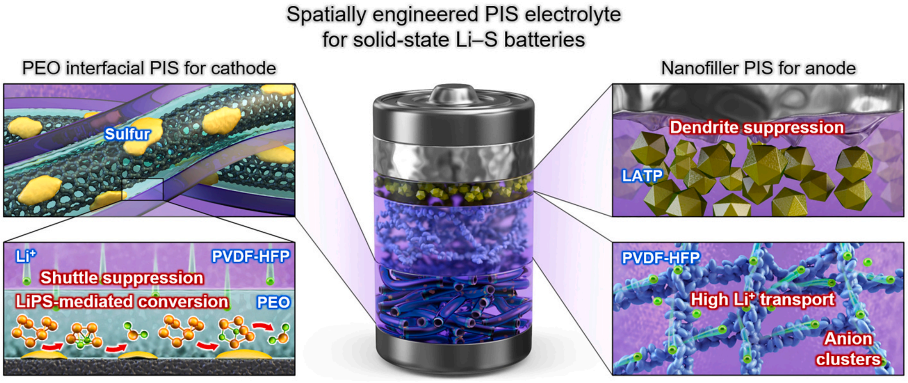

Fig. 1. Schematic illustration of a region-specific PIS architecture. A PEO-based PIS interlayer at the cathode promotes LiPS-mediated conversion while blocking shuttle migration. At the anode, LATP-reinforced PVDF-HFP PIS maintains stable Li contact and suppresses dendrites. The PVDF-HFP PIS bulk conducts Li$^+$ through anion-cluster networks.

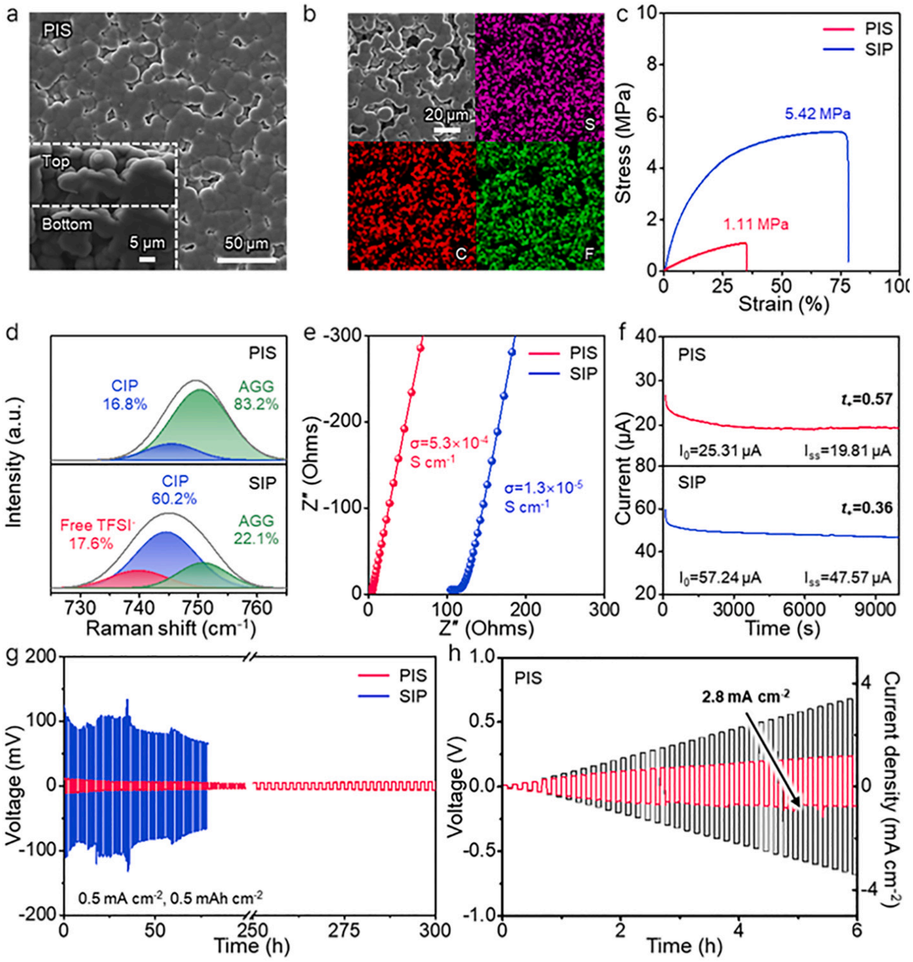

Fig. 2. Structural and electrochemical properties of PVDF-HFP–PIS electrolytes. (a) SEM images of the PIS film. (b) EDS mapping of elemental distributions in PIS. (c) Tensile strength of PIS and SIP films. (d) Raman spectra of PIS and SIP. (e) Ionic conductivity of PIS and SIP. (f) Li^+ transference numbers of PIS and SIP. (g) Li|Li symmetric cell cycling performance with PIS and SIP electrolytes. (h) CCD of PIS.

film tearing, confirming their interfacial compatibility (Fig. S8). Notably, the ionic conductivity of the PEO/PVDF-HFP double layer remains comparable to that of pristine PVDF-HFP PIS, which is attributed to ion transport in both systems being mediated through a common excess LiTFSI salt network (Fig. S9).

To directly assess the stabilization of LiPS provided by the PEO matrix, we analyzed the thermal reaction between sulfur (S_8) and lithium sulfide (Li_2S) at 55 °C at the polymer interface. This method enabled the evaluation of LiPS formation within the polymer medium. The generation of LiPS indicates that the polymer medium stabilizes LiPS and enables LiPS-mediated reaction pathways. During the thermal reaction, PEO films enclosing the sulfur–Li_2S mixture developed a distinct red coloration (Fig. 3d), indicative of LiPS formation, whereas PVDF-HFP films retained their original yellow color, demonstrating the absence of LiPS formation (Fig. 3e). X-ray photoelectron spectroscopy (XPS) corroborated these observations. The S 2p spectrum of the PVDF-HFP sample showed only peaks at ~164.6 eV and ~ 160.2 eV, corresponding to elemental sulfur and Li_2S, respectively (Fig. 3f). [42] In contrast, the PEO sample exhibited additional peaks at ~161.7 eV and ~ 163.1 eV, assigned to terminal sulfur and bridging sulfur species of higher-order polysulfides. [43] Furthermore, peaks observed at ~168–170 eV were attributed to oxidized sulfur species ($–SO_x$), which demonstrates that LiPS is stabilized within the PEO matrix through coordination with ether oxygen atoms. [44] These results were further validated at room temperature, where S/Li_2S reactions showed consistent LiPS formation in PEO and its absence in PVDF-HFP, as confirmed by both optical observation and XPS analysis (Figs. S10 and 11).

The role of the PVDF-HFP layer in suppressing LiPS transport was investigated using an H-type diffusion cell (H-cell), where the polymer film acted as a separator to monitor LiPS permeation driven by a concentration gradient. An electrolyte containing LiPS was placed on one side of the cell, while the opposite side was isolated by the polymer film (Fig. 3g). No detectable LiPS crossover was observed through the PVDF-HFP membrane for at least 4 h, indicating effective suppression of polysulfide migration. In contrast, measurable LiPS diffusion was observed across the PEO film. This behavior is attributed to the poor coordination of the –C–F bonds in PVDF-HFP, whereas the –C–O–C segments in PEO strongly coordinate with Li^+ and thereby facilitate LiPS dissolution. [45,46] DFT calculations further corroborated this difference, confirming favorable LiPS solvation in PEO over PVDF-HFP (Fig. S14).

Cyclic voltammetry (CV) analysis demonstrated the regulation of redox behavior in PIS cells. [47] The PEO-modified cathode PIS cell exhibited two cathodic peaks at 2.2–2.3 V and 2.0–2.1 V, along with a single anodic peak at 2.3–2.4 V, closely resembling the stepwise redox profile typically observed in liquid-electrolyte Li—S systems (Fig. 3h). [48,49] In contrast, the pristine cathode PIS cell displayed a single cathodic peak at ~1.95 V and a single anodic peak at ~2.3 V. This distinct behavior indicates that PEO domains enabled sulfur conversion through LiPS formation, whereas the PIS cell proceeded via a direct solid–solid reduction pathway without LiPS intermediates. Furthermore, comparison of peak intensities and polarization revealed that the PEO-cathode PIS cell exhibited stronger peaks with lower polarization,

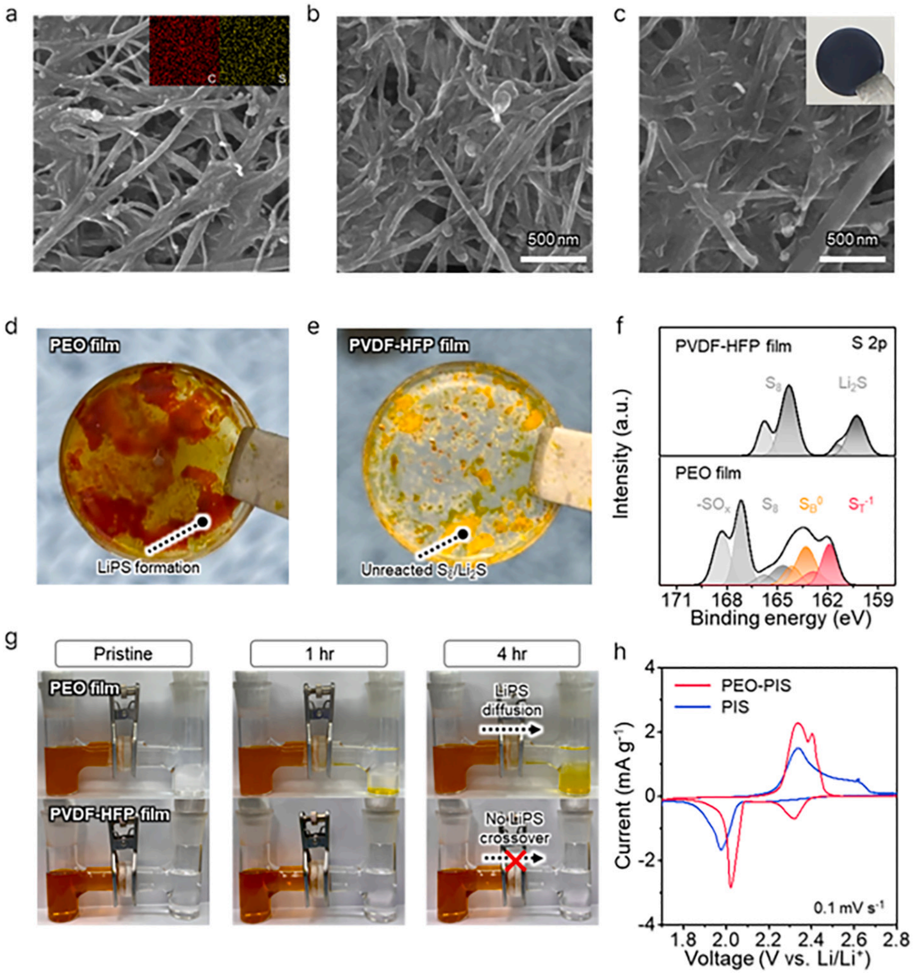

Fig. 3. Structural and electrochemical properties of PEO-modified sulfur cathodes. (a) SEM image and EDS mapping of the sulfur cathode. (b) SEM image after deposition of the PEO-containing interfacial film. (c) SEM image after infiltration of the PVDF-HFP–based PIS film. (d) Optical image showing LiPS formation in the PEO film. (e) Optical image of the PVDF-HFP film showing no LiPS formation. (f) S 2p XPS spectra of PVDF-HFP and PEO films. (g) H-type diffusion cell test comparing LiPS permeation across PVDF-HFP and PEO films. (h) Cyclic voltammetry of PIS cells with PEO-modified and pristine sulfur cathodes.

indicative of enhanced sulfur redox kinetics compared with the PIS cell.

PIS electrolytes inherently exhibit limited mechanical strength due to their high salt content, which compromises their ability to suppress lithium dendrite growth. [50] Prior studies suggest that a mechanical strength of at least 2–5 MPa is required to inhibit dendrite propagation. [45,51] To address this, we incorporated 50 wt% lithium aluminum titanium phosphate (LATP, $Li_{1-x}Al_xTi_{2-x}(PO_4)_3$) nanofillers into the PIS matrix to create an anode-facing electrolyte (Fig. S12). In addition to mechanical reinforcement, LATP contributes to lithium-ion transport by providing fast-conducting pathways and facilitating interfacial ion migration at the polymer–ceramic interface. [52]

SEM confirmed the uniform dispersion of LATP nanofillers within the PIS matrix, further supported by EDS mapping of Al, Ti, and P (Fig. 4a and b and Fig. S13). Such interfacial compatibility effectively prevents direct contact between LATP and lithium metal, thereby suppressing side reactions associated with the reductive instability of LATP. Mechanical testing showed that the Nanofiller-PIS composite achieved a tensile strength of 2.94 MPa, representing a 165% increase over PIS and falling within the dendrite-suppressing threshold (Fig. 4c). EIS measurements indicated a moderate increase in ionic conductivity, from 5.3×10^{-4} S cm^{-1} for the PIS to 6.0×10^{-4} S cm^{-1} for Nanofiller-PIS, attributed to reduced polymer crystallinity and increased free volume for ion migration (Fig. S15). [53,54] Temperature-dependent EIS measurements showed that the activation energy for Li^+ transport in Nanofiller–PIS was slightly lower (0.09 eV) than in PIS (0.11 eV) (Fig. S16). [55] The Li^+ transference number of Nanofiller–PIS was 0.59, slightly higher than that of PIS (0.57) (Fig. S17).

Enhanced mechanical properties directly translated into improved electrochemical performance. Li|Li symmetric cells employing PIS or Nanofiller–PIS electrolyte films were tested at 0.5 mA cm^{-2} and 0.5 mAh cm^{-2}: the PIS cell exhibited increasing overpotential and short-circuited after 320 h, whereas the Nanofiller–PIS cell maintained low overpotential and stable cycling for more than 350 h (Fig. 4d). SEM analysis after 300 h revealed smoother Li surfaces with Nanofiller-PIS, evidencing suppressed dendrite growth (Fig. S18). Under higher current densities, the Nanofiller–PIS cell sustained stable operation for more than 600 h at 1.5 mA cm^{-2} and 0.75 mAh cm^{-2}, and over 800 cycles at 2.0 mA cm^{-2} and 1.0 mAh cm^{-2}, maintaining stable voltage profiles (Fig. 4e and Fig. S19). This long-term stability also indicates that LATP does not undergo parasitic reactions with the Li anode or the lithium salt (Fig. S20). CCD measurements showed that the Nanofiller–PIS remained stable up to 3.5 mA cm^{-2} before voltage collapse, corresponding to a 25% improvement in durability compared with PIS (Fig. 4f). The improved electrochemical performance with Nanofiller–PIS is further supported by Li morphology: lithium plated with Nanofiller–PIS formed a dense and smooth surface (Fig. 4g, top), whereas PIS resulted in a rough and porous morphology, indicative of unstable deposition (Fig. 4g, bottom).

EIS of Li|Li symmetric cells, measured hourly at 0.5 mA cm^{-2}, showed a progressive decrease in interfacial resistance during cycling,

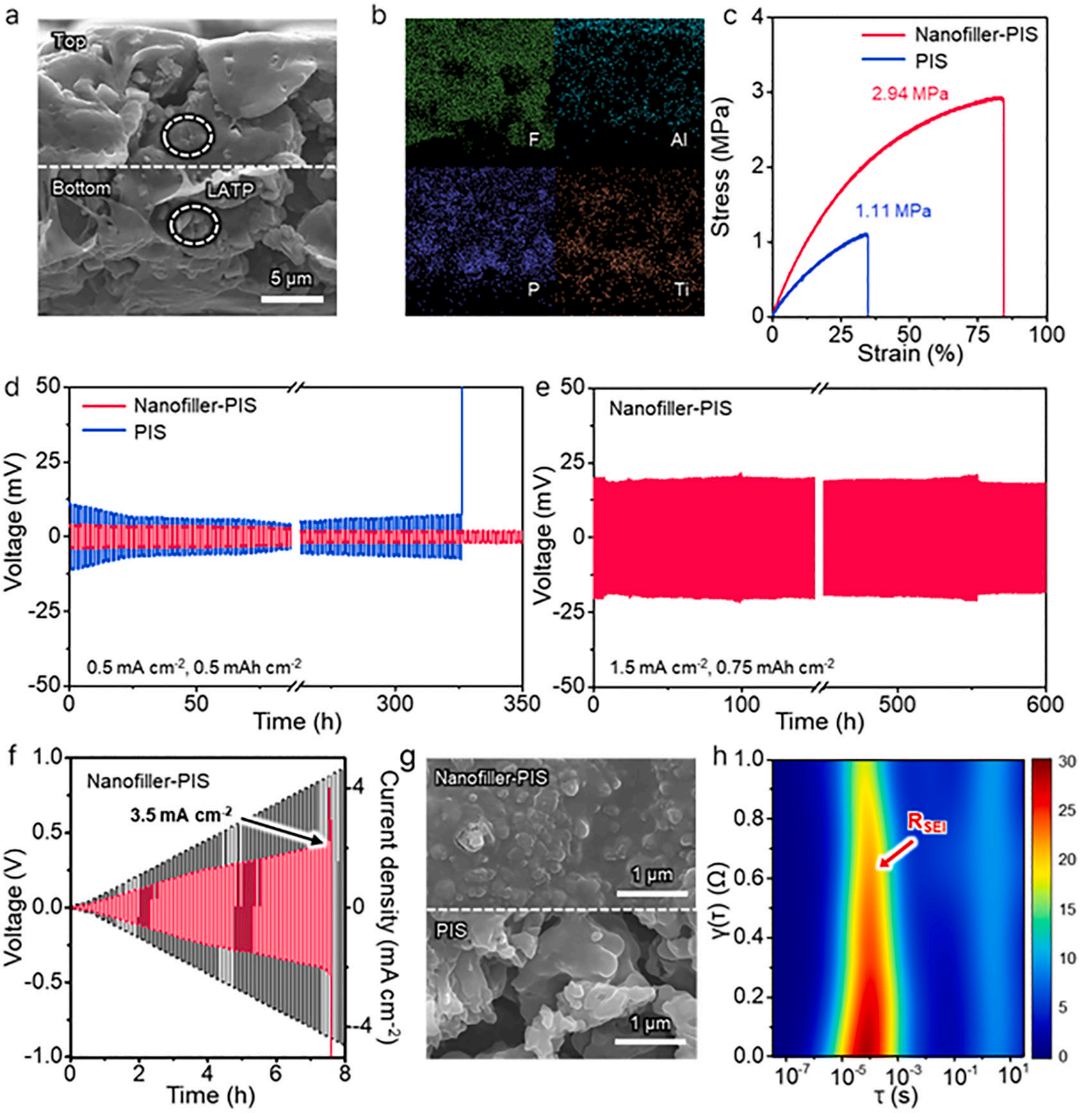

Fig. 4. Structural and electrochemical properties of Nanofiller–PIS electrolytes. (a) Cross-sectional SEM image of Nanofiller-PIS. (b) EDS image of Nanofiller-PIS. (c) Tensile strength of Nanofiller-PIS and PIS. (d, e) Li symmetric data of Nanofiller-PIS and PIS Raman spectrums of PIS, SIP. (f) Critical current density of PIS and SIP. (g) SEM images of Li electrodes after 300 h of Li|Li symmetric cycling with PIS (bottom) and Nanofiller–PIS (top) electrolytes. (h) DRT analysis of PIS and Nanofiller–PIS cells.

indicating stabilization of the Li metal–electrolyte interface (Fig. S21). These results were corroborated by distribution of relaxation time (DRT) analysis, which decomposed resistance contributions as a function of relaxation time (τ) (Fig. 4h and Fig. S22). [56,57] The sharp peak profile indicates a uniform and homogeneous interfacial layer, consistent with the formation of an inorganic-rich, ionically conductive solid-electrolyte interface (SEI). [56] Moreover, the Nanofiller–PIS cell exhibited a peak at shorter τ values, reflecting a lower charge-transfer barrier at the electrolyte–Li interface and confirming that LATP incorporation maintains interfacial stability. [30]

We assembled Li—S cells employing a region-specific PIS electrolyte, featuring a PEO-modified cathode and a Nanofiller-modified anode—referred to as the dual-modified cell (PEO-C–NF-A cell). For comparison, we also fabricated a PEO-C cell, where the cathode was modified with PEO while the anode employed pristine PVDF-HFP PIS, as well as an NF-A cell, in which the anode contained Nanofillers while the cathode employed pristine PVDF-HFP PIS.

Galvanostatic charge–discharge profiles at 0.05C are shown in Fig. 5a. The NF-A cell displayed a sloped discharge curve with gradual voltage decay, indicative of a direct solid-state sulfur conversion process without LiPS mediation. In contrast, both the PEO-C–NF-A cell and PEO-C cells exhibited two well-defined voltage plateaus at ~2.1 V and ~ 2.3 V, resembling profiles of conventional liquid-electrolyte systems. [58] This behavior is attributed to the PEO-rich cathode interfacial layer, which facilitates stepwise sulfur reduction via LiPS intermediates (Fig. S23).

Among the three configurations, the PEO-C–NF-A cell delivered the highest initial discharge capacity of 1180 mAh g^{-1}—approximately 1.5× that of the NF-A cell (790 mAh g^{-1})—highlighting the benefit of LiPS-mediated conversion. It also outperformed the PEO-C cell (880 mAh g^{-1}) by 34%, a performance gain attributed to reduced interfacial resistance and suppressed overpotential at the anode via Nanofiller-induced stabilization.

Rate capability was evaluated by stepwise increasing the C-rate from 0.1 to 0.5C (Fig. 5b and c and Fig. S24). [18,59–62] Under a fivefold increase in current (0.1 to 0.5C), the PEO-C–NF-A and PEO-C cells retained 45% and 34% of their initial capacities, respectively. For PEO-C–NF-A, the galvanostatic charge–discharge profiles from 0.1 to 0.5C maintained two well-defined voltage plateaus, which indicated that the stepwise LiPS-mediated conversion pathway remained operative at

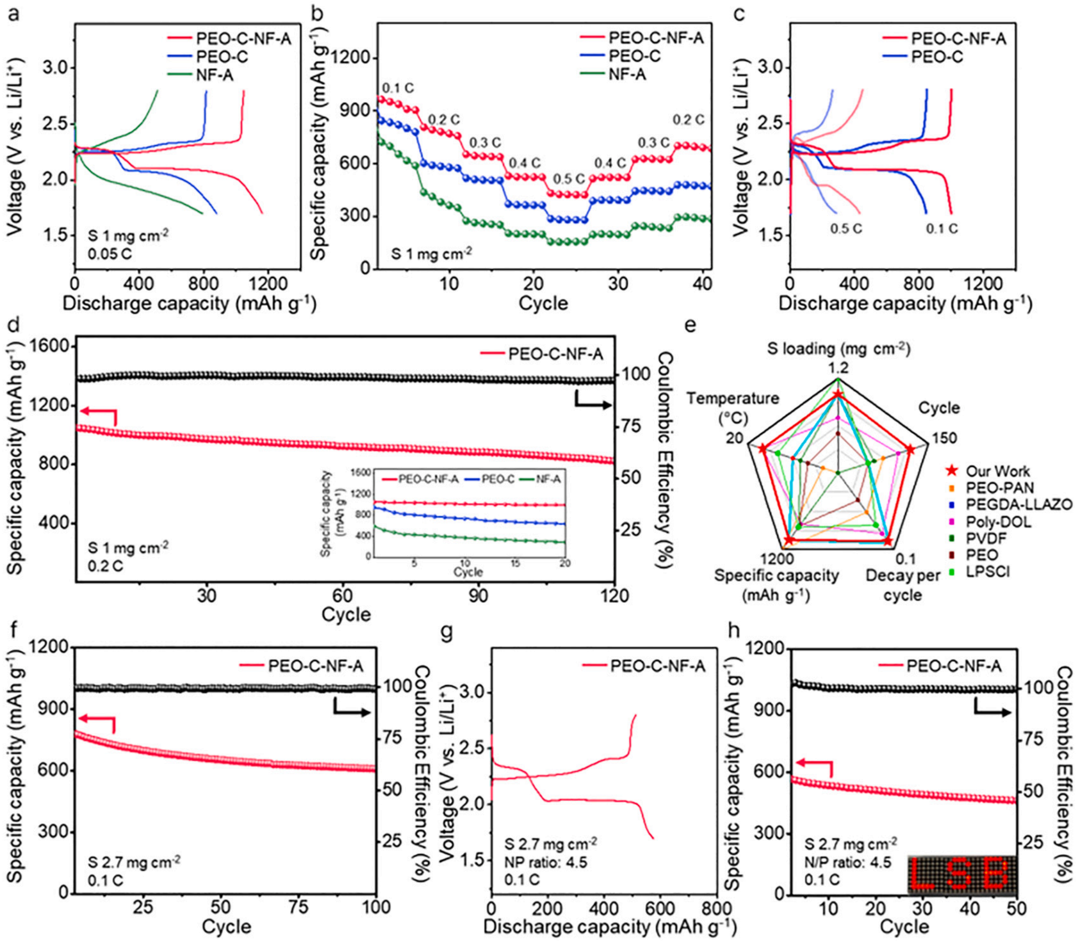

Fig. 5. Electrochemical performance of solid Li—S cells. (a) Charge–discharge profiles at 0.05C with 1 mg cm^{-2} sulfur loading. (b) Rate capability tested across various C-rates. (c) Charge-discharge profiles of the PEO-C–NF-A cell from 0.1 to 0.5C. (d) Cycling stability of the PEO–C–NF–A cell at 0.2C with 1 mg cm^{-2} sulfur. (e) Benchmarking plot comparing our work with previous studies. (f) Cycling capacity and Coulombic efficiency of a cell with 2.7 mg cm^{-2} sulfur loading at 0.1C. (g) Charge-discharge profiles and (h) cycling performance of a cell with 2.7 mg cm^{-2} sulfur loading, N/P ratio of 4.5, at 0.1C; the inset shows the full cell powering LED display.

higher rates; by contrast, NF-A retained only 21% and exhibited rapid capacity decay, consistent with slower direct solid–solid conversion kinetics. For comparison, previously reported solid-state Li—S systems typically retain ~35–45% of their initial capacity when the C-rate increases fivefold, consistent with values of ~42% for PEO–acetamide electrolytes, ~38% for PVDF-HFP gels, and ~ 43% for PEO–LLZO composites. [63–66] The PEO-modified architecture achieved comparable or higher retention (~45%) over the same C-rate increase, suggesting higher rate tolerance.

Long-term cycling at 0.2C (Fig. 5d and Fig. S25) further validated the enhanced durability of the PEO-C–NF-A cell. It maintained 78% of its initial capacity after 120 cycles, corresponding to an average capacity retention above 99% per cycle, while the Coulombic efficiency was consistently maintained at 99%. This level of CE is unlikely to arise from polysulfide shuttle and may instead reflect interfacial processes such as SEI formation (Fig. S26). A performance comparison with previously reported solid-state Li—S cells revealed that the PEO-C–NF-A cell achieved superior capacity and cycle life at relatively high C-rates (Fig. 5e and Table S1). [17,18,22,60,61,67]

To evaluate performance under practical conditions, the PEO-C–NF-A cell was tested with a sulfur loading of 2.7 mg cm^{-2} at 0.1C (Fig. 5f). The cell delivered an initial capacity of 780 mAh g^{-1} with a moderate decay rate of 0.25% per cycle. Few prior studies demonstrate stable cycling above 2 mg cm^{-2}. For example, cells using PEO–PGA electrolytes delivered 606 mAh g^{-1}, and those with PEO-acetamide electrolytes delivered 587 mAh g^{-1}—both lower than the dual-modified benchmark. [59,63] Finally, we assembled a full cell with an N/P ratio of 4.5 and a sulfur loading of 2.7 mg cm^{-2}. The full-cell galvanostatic profile showed well-defined charge–discharge plateaus with moderate voltage hysteresis, consistent with sustained sulfur-conversion reactions under a constrained lithium inventory (Fig. 5g). At 0.1C, this configuration delivered an initial discharge capacity of 570 mAh g^{-1} and retained 80% of its capacity over 50 cycles, corresponding to a per-cycle fade rate of 0.43%, while maintaining a Coulombic efficiency of ~99.5% (Fig. 5g-h). To further evaluate practical viability, cells were tested under more stringent conditions: at S 3.0 mg cm^{-2} (E/S 7.0, N/P 2.9) and S 3.2 mg cm^{-2} (E/S 6.6, N/P 2.5), the cells delivered initial capacities of 920 and ~ 800 mAh g^{-1} at 0.05C, respectively (Fig. S27). As a proof-of-concept demonstration of power output, the full cell also drove a light-emitting diode display (inset of Fig. 5h).

3. Conclusions

This study resolves the solid-state paradox of lithium–sulfur batteries by introducing a spatially engineered PIS electrolyte architecture that combines polysulfide suppression with rapid sulfur redox kinetics. The PVDF-HFP PIS bulk electrolyte provides high ionic conductivity (5.3 × 10^{-4} S cm^{-1}) and a Li^{+} transference number of 0.59, while effectively limiting polysulfide crossover. At the cathode, a PEO-rich interfacial layer stabilizes LiPS intermediates and enables stepwise sulfur conversion, with two distinct voltage plateaus and reduced polarization. At the anode, Nanofiller-PIS enhances mechanical robustness, suppresses dendrite propagation, and sustains stable Li plating/stripping for over 350 h. Full cells with this region-specific architecture delivered discharge capacities of up to 1180 mAh g^{-1} (S 1 mg cm^{-2}, 0.05C), retained 78% of their capacity after 120 cycles at 0.2C, and, with a sulfur loading of 2.7 mg cm^{-2} and an N/P ratio of 4.5, achieved 80% retention after 50 cycles. By integrating bulk ion transport, interfacial kinetics, and mechanical durability, this work establishes a scalable and mechanistically informed design principle for advancing high-performance solid-state Li—S batteries.

4. Experimental section

4.1. Preparation of electrolytes and cathodes

Sulfur (Alfa Aesar), MWCNT (Sigma Aldrich), Super P (Thermo Scientific), lithium bis(trifluoromethanesulfonyl)imide (LiTFSI, Sigma Aldrich), LA132 (Thermo Scientific), Poly(vinylidene fluoride-*co*-hexafluoropropylene) (PVDF-HFP, Sigma-Aldrich), Poly(ethylene Oxide) (PEO, Sigma Aldrich), Lithium Aluminum Titanium Phosphate (LATP, Sigma-Aldrich), *N*,*N*-Dimethylformamide (DMF, Sigma-Aldrich), Acetonitrile (ACN, Sigma-Aldrich), and 1,2-dimethoxyethane (DME, Sigma-Aldrich) were purchased from commercial sources. PIS electrolytes were prepared by mixing PVDF-HFP with LiTFSI at a 1:1 mass ratio, dissolving the mixture in DMF, and vacuum-drying at 60 °C for 24 h to obtain films approximately 20 μm thick. SIP electrolytes were prepared using 20 wt% LiTFSI in PVDF-HFP following the same casting/drying process. For the cathode interfacial layer, a PEO/LiTFSI solution (1.3:1 wt% in ACN) was coated onto the sulfur cathode and dried to form a thin PEO interfacial layer. For the anode-side electrolyte, Nanofiller-PIS was prepared by incorporating 50 wt% LATP into the PIS mixture, followed by the same casting/drying process used for PIS. S/CNT composites were prepared by mixing sulfur and MWCNT through the conventional melt-diffusion method. Sulfur cathodes were produced by casting a slurry of S/CNT composite, Super P, and LA132 onto Al foil, followed by drying in a vacuum oven at 60 °C for 24 h.

4.2. Cell assembly and electrochemical tests

All electrochemical measurements were carried out at 30 °C unless otherwise specified. CR2032-type Li—S coin cells were assembled in an Ar-filled glovebox (O_2, H_2O < 0.1 ppm). Four configurations were studied: PVDF-HFP PIS cells (PIS both sides), PEO-C cells (PEO-modified PIS cathode, PIS anode), NF-A cell (Nanofiller-PIS at anode, PIS elsewhere), and PEO-C-NF-A cells (PEO-cathode and Nanofiller-anode). Sulfur loading was 1–3 mg cm^{-2} and Li-metal foils served as anodes. Electrochemical impedance spectroscopy (EIS) was performed using an impedance analyzer (Versastat, AMETEK), scanning frequencies from 0.1 Hz to 1 MHz with a voltage amplitude set at 10 mV. Ionic conductivity was calculated from bulk resistance, and Li^+ transference number (t_+) was measured by the Bruce–Vincent method using 10 mV polarization combined with pre/post impedance spectra. Critical current density (CCD) was determined by stepwise increases in current (0.1 mA cm^{-2} h^{-1}) until voltage collapse. Galvanostatic cycling of Li—S cells was performed in the voltage range of 1.7–2.8 V at rates of 0.1–0.5C using a Maccor 4300 Battery Test System. Electrochemical performance data were obtained from an average of three experimental runs (error bars and standard deviation were not shown for convenience), and the specific capacity was calculated based on the mass of sulfur in the cathode, employing a theoretical capacity of 1675 mAh g^{-1}. This calculation was predicated on the average coulombic efficiency (CE) value of samples being greater than 99%. Cyclic voltammetry is conducted under the same voltage range at a test temperature of 30 °C. Symmetric Li|electrolyte|Li cells were cycled at 0.5 mA cm^{-2} with 0.5 mAh cm^{-2} areal capacity, and EIS was collected hourly. Distribution of relaxation time (DRT) analysis (DRTtools) was used to separate the bulk, grain boundary, and interfacial contributions.

4.3. Mechanical and interfacial tests

Tensile strength of electrolyte membranes was measured using a universal testing machine. Strips (5 × 20 mm) were tested at a crosshead speed of 5 mm min^{-1} at room temperature, and average values were reported from multiple specimens. To probe LiPS stabilization, sulfur/Li_2S (Merck) mixtures were sandwiched between polymer films (PEO or PVDF-HFP) and thermally treated at 55 °C for 24 h, followed by color observation and XPS analysis. LiPS permeation was assessed using H-type diffusion cells containing Li_2S_6 solution on one side and pure solvent on the other, separated by polymer membranes; crossover was monitored by UV–Vis spectroscopy.

4.4. Structural characterization

Morphology and composition were examined by field-emission scanning electron microscopy (FE-SEM, JSM-7100F) equipped with EDS. Differential scanning calorimetry (DSC) was carried out at 10 °C min^{-1} under N_2. Raman spectra were acquired in the range of 200–1600 cm^{-1} using an excitation wavelength of 532 nm (Horiba-iHR550). X-ray photoelectron spectroscopy (XPS) data were collected using a Leybold spectrometer equipped with an Al Kα monochromatic beam (1486.6 eV, 150 W input power, ESCALAB250 XPS system, Theta Probe XPS system). It was performed to analyze sulfur species, with C 1 s (284.8 eV) as reference.

4.5. Density functional theory calculations

All calculations were conducted using the Quantum ESPRESSO package, which is based on density functional theory. The projector augmented wave (PAW) method and the Generalized Gradient Approximation (GGA) with the Perdew–Burke–Ernzerhof (PBE) exchange-correlation function were utilized. A plane-wave basis set with a cutoff energy of 95 Ry was employed. All DFT calculations were selected according to the Monkhorst-Pack scheme to perform Brillouin zone integration. For structure optimization, all ions were relaxed until the maximum force on each ion was less than 0.005 eV $Å^{-1}$. The solvation potential (ΔΔG) of Li_2S_6 with PEO and PVDF-HFP was calculated by subtracting the cohesive energy of Li_2S_6 from the solvation energy with each polymer.

CRediT authorship contribution statement

Haeli Lee: Methodology, Formal analysis, Data curation. **Nagyeong Shin:** Formal analysis, Data curation. **Taehyun Kim:** Formal analysis, Data curation. **Minho Jung:** Formal analysis, Data curation. **Seung Gi Jung:** Formal analysis, Data curation. **Jinhan Cho:** Validation. **Holger Althues:** Validation. **Jun Hyuk Moon:** Writing – review & editing, Writing – original draft, Supervision, Project administration, Funding acquisition, Conceptualization.

Declaration of competing interest

The authors declare that they have no known competing financial interests or personal relationships that could have appeared to influence the work reported in this paper.

Acknowledgments

This work was supported by the National Research Foundation of Korea (2025-00559443, 2025-02214734, 2025-25433916) and the Industrial Technology Innovation Program funded by the Ministry of Trade, Industry and Energy, Republic of Korea (P268600148).

Appendix A. Supplementary data

Supplementary data to this article can be found online at https://doi.org/10.1016/j.cej.2026.175471.

Data availability

Data will be made available on request.

References

[1] A. Manthiram, Y. Fu, S.-H. Chung, C. Zu, Y.-S. Su, Rechargeable lithium–sulfur batteries, Chem. Rev. 114 (23) (2014) 11751–11787.
[2] Z.W. Seh, Y. Sun, Q. Zhang, Y. Cui, Designing high-energy lithium–sulfur batteries, Chem. Soc. Rev. 45 (20) (2016) 5605–5634.
[3] P.G. Bruce, S.A. Freunberger, L.J. Hardwick, J.-M. Tarascon, Li–O2 and Li–S batteries with high energy storage, Nat. Mater. 11 (1) (2012) 19–29.
[4] S. Zhang, K. Ueno, K. Dokko, M. Watanabe, Recent advances in electrolytes for lithium–sulfur batteries, Adv. Energy Mater. 5 (16) (2015) 1500117.
[5] B. Deng, F. Scheiba, A. Zuo, S. Indris, H. Li, H. Radinger, A. Grimm, C. Njel, Sulfur Distribution Analysis in Lithium– Sulfur Cathode via Confined Inverse Vulcanization in Carbon Frameworks, Adv. Energy Mater. 15 (9) (2025) 2402996.
[6] Y. Liu, L. Xu, Y. Yu, M. He, H. Zhang, Y. Tang, F. Xiong, S. Gao, A. Li, J. Wang, Stabilized Li-S batteries with anti-solvent-tamed quasi-solid-state reaction, Joule 7 (9) (2023) 2074–2091.
[7] L. Peng, Z. Wei, C. Wan, J. Li, Z. Chen, D. Zhu, D. Baumann, H. Liu, C.S. Allen, X. Xu, A fundamental look at electrocatalytic sulfur reduction reaction, Nat. Catal. 3 (9) (2020) 762–770.
[8] X. Sun, Y. Qiu, B. Jiang, Z. Chen, C. Zhao, H. Zhou, L. Yang, L. Fan, Y. Zhang, N. Zhang, Isolated Fe-Co heteronuclear diatomic sites as efficient bifunctional catalysts for high-performance lithium-sulfur batteries, Nat. Commun. 14 (1) (2023) 291.
[9] D. Wang, L.-J. Jhang, R. Kou, M. Liao, S. Zheng, H. Jiang, P. Shi, G.-X. Li, K. Meng, D. Wang, Realizing high-capacity all-solid-state lithium-sulfur batteries using a low-density inorganic solid-state electrolyte, Nat. Commun. 14 (1) (2023) 1895.
[10] F. Pei, L. Wu, Y. Zhang, Y. Liao, Q. Kang, Y. Han, H. Zhang, Y. Shen, H. Xu, Z. Li, Interfacial self-healing polymer electrolytes for long-cycle solid-state lithium-sulfur batteries, Nat. Commun. 15 (1) (2024) 351.
[11] Q. Zhu, C. Ye, D. Mao, Solid-state electrolytes for lithium–sulfur batteries: challenges, progress, and strategies, Nanomaterials 12 (20) (2022) 3612.
[12] C. Wang, J.T. Kim, C. Wang, X. Sun, Progress and prospects of inorganic solid-state electrolyte-based all-solid-state pouch cells, Adv. Mater. 35 (19) (2023) 2209074.
[13] J. Liu, Y. Zhou, T. Yan, X.P. Gao, Perspectives of high-performance Li–S battery electrolytes, Adv. Funct. Mater. 34 (4) (2024) 2309625.
[14] S. Liu, L. Zhou, T. Zhong, X. Wu, K. Neyts, Sulfide/Polymer Composite Solid-State Electrolytes for All-Solid-State Lithium Batteries, Adv. Energy Mater. 14 (48) (2024) 2403602.
[15] B. Hu, J. Xu, Z. Fan, C. Xu, S. Han, J. Zhang, L. Ma, B. Ding, Z. Zhuang, Q. Kang, Covalent organic framework based lithium–sulfur batteries: materials, interfaces, and solid-state electrolytes, Adv. Energy Mater. 13 (10) (2023) 2203540.
[16] Z. Yu, B. Singh, Y. Yu, L.F. Nazar, Suppressing argyrodite oxidation by tuning the host structure for high-areal-capacity all-solid-state lithium–sulfur batteries, Nat. Mater. (2025) 1–9.
[17] R. Fang, H. Xu, B. Xu, X. Li, Y. Li, J.B. Goodenough, Reaction mechanism optimization of solid-state Li–S batteries with a PEO-based electrolyte, Adv. Funct. Mater. 31 (2) (2021) 2001812.
[18] X. Meng, Y. Liu, Y. Ma, Y. Boyjoo, J. Liu, J. Qiu, Z. Wang, Diagnosing and correcting the failure of the solid-state polymer electrolyte for enhancing solid-state lithium–sulfur batteries, Adv. Mater. 35 (22) (2023) 2212039.
[19] S. Lang, S.-H. Yu, X. Feng, M.R. Krumov, H.D. Abruña, Understanding the lithium–sulfur battery redox reactions via operando confocal Raman microscopy, Nat. Commun. 13 (1) (2022) 4811.
[20] D. Cao, X. Sun, F. Li, S.M. Bak, T. Ji, M. Geiwitz, K.S. Burch, Y. Du, G. Yang, H. Zhu, Understanding electrochemical reaction mechanisms of sulfur in all-solid-state batteries through Operando and theoretical studies, Angew. Chem. 62 (20) (2023) e202302363.
[21] D.L. Melvin, M. Siniscalchi, D. Spencer-Jolly, B. Hu, Z. Ning, S. Zhang, J. Bu, S. Marathe, A. Bonnin, J. Ihli, High plating currents without dendrites at the interface between a lithium anode and solid electrolyte, Nat. Energy (2025) 1–10.
[22] J. Zhou, M.L. Holekevi Chandrappa, S. Tan, S. Wang, C. Wu, H. Nguyen, C. Wang, H. Liu, S. Yu, Q.R. Miller, Healable and conductive sulfur iodide for solid-state Li–S batteries, Nature 627 (8003) (2024) 301–305.
[23] Y. Zhang, L. Gao, H. Zheng, H. Zhao, G. Zhao, Advancing sulfide solid electrolytes via green Li2S synthesis, Nat. Commun. 16 (1) (2025) 9981.
[24] Z. Li, S. Peng, L. Wei, X. Guo, Why Will Polymers Win the Race for Solid-State Batteries? Adv. Sci. 12 (36) (2025) e10481.
[25] W. Liu, C. Yi, L. Li, S. Liu, Q. Gui, D. Ba, Y. Li, D. Peng, J. Liu, Designing polymer-in-salt electrolyte and fully infiltrated 3D electrode for integrated solid-state lithium batteries, Angew. Chem. 133 (23) (2021) 13041–13050.
[26] P. Li, Y. Huang, Y. Yu, X. Ma, Z. Wang, G. Shao, Recent advances and future prospects for PVDF-based solid polymer electrolytes, J. Power Sources 628 (2025) 235855.
[27] C. Angell, C. Liu, E. Sanchez, Rubbery solid electrolytes with dominant cationic transport and high ambient conductivity, Nature 362 (6416) (1993) 137–139.
[28] D.G. Mackanic, W. Michaels, M. Lee, D. Feng, J. Lopez, J. Qin, Y. Cui, Z. Bao, Crosslinked poly (tetrahydrofuran) as a loosely coordinating polymer electrolyte, Adv. Energy Mater. 8 (25) (2018) 1800703.
[29] G.-R. Zhu, Q. Zhang, Q.-S. Liu, Q.-Y. Bai, Y.-Z. Quan, Y. Gao, G. Wu, Y.-Z. Wang, Non-flammable solvent-free liquid polymer electrolyte for lithium metal batteries, Nat. Commun. 14 (1) (2023) 4617.
[30] J. Lu, B. Sheng, M. Chen, M. Xu, Y. Zhang, S. Zhao, Q. Zhou, C. Li, B. Wang, J. Liu, Localized high concentration polymer electrolyte enabling room temperature solid-state lithium metal batteries with stable LiF-rich interphases, Energy Storage Mater. 71 (2024) 103570.
[31] H. Tu, L. Li, Y. Hu, Y. Zhang, Y. Wang, W. Huang, Z. Ren, H. Lin, M. Liu, Non-flammable liquid polymer-in-salt electrolyte enabling secure and dendrite-free lithium metal battery, Chem. Eng. J. 434 (2022) 134647.
[32] Q. Zhou, J. Ma, S. Dong, X. Li, G. Cui, Intermolecular chemistry in solid polymer electrolytes for high-energy-density lithium batteries, Adv. Mater. 31 (50) (2019) 1902029.
[33] Q. Cheng, L. Wei, Z. Liu, N. Ni, Z. Sang, B. Zhu, W. Xu, M. Chen, Y. Miao, L.-Q. Chen, Operando and three-dimensional visualization of anion depletion and lithium growth by stimulated Raman scattering microscopy, Nat. Commun. 9 (1) (2018) 2942.
[34] J. Evans, C.A. Vincent, P.G. Bruce, Electrochemical measurement of transference numbers in polymer electrolytes, Polymer 28 (13) (1987) 2324–2328.
[35] B.-J. Lee, C. Zhao, J.-H. Yu, T.-H. Kang, H.-Y. Park, J. Kang, Y. Jung, X. Liu, T. Li, W. Xu, Development of high-energy non-aqueous lithium-sulfur batteries via redox-active interlayer strategy, Nat. Commun. 13 (1) (2022) 4629.
[36] R. Xu, S. Tang, X. Li, H. Guo, Z. Wang, G. Li, J. Wang, H. Duan, W. Peng, G. Yan, Relieving concentration polarization through electrode structure optimization based on direct current internal resistance decomposition, Energy Storage Mater. 75 (2025) 104013.
[37] Z. Song, F. Chen, M. Martinez-Ibañez, W. Feng, M. Forsyth, Z. Zhou, M. Armand, H. Zhang, A reflection on polymer electrolytes for solid-state lithium metal batteries, Nat. Commun. 14 (1) (2023) 4884.
[38] Y. Liu, X. Meng, Z. Wang, J. Qiu, Development of quasi-solid-state anode-free high-energy lithium sulfide-based batteries, Nat. Commun. 13 (1) (2022) 4415.
[39] J.T. Kim, A. Rao, H.-Y. Nie, Y. Hu, W. Li, F. Zhao, S. Deng, X. Hao, J. Fu, J. Luo, Manipulating Li2S2/Li2S mixed discharge products of all-solid-state lithium sulfur batteries for improved cycle life, Nat. Commun. 14 (1) (2023) 6404.
[40] J. Guo, Q. Yang, Y. Dou, X. Ba, W. Wei, J. Liu, Shelf life of lithium–sulfur batteries under lean electrolytes: status and challenges, Energy Environ. Sci. 17 (5) (2024) 1695–1724.
[41] R. Xiao, Z. Qu, J. Ren, G. Wang, Z. Sun, F. Li, Current status and future prospects of solid-state lithium–sulfur batteries: a focus on reaction and interface engineering, Adv. Energy Mater. (2025) 2501926.
[42] X. Liang, C. Hart, Q. Pang, A. Garsuch, T. Weiss, L.F. Nazar, A highly efficient polysulfide mediator for lithium–sulfur batteries, Nat. Commun. 6 (1) (2015) 5682.
[43] Q. Pang, D. Kundu, M. Cuisinier, L. Nazar, Surface-enhanced redox chemistry of polysulphides on a metallic and polar host for lithium-sulphur batteries, Nat. Commun. 5 (1) (2014) 4759.
[44] M. Seredych, A.V. Tamashausky, T.J. Bandosz, Graphite oxides obtained from porous graphite: the role of surface chemistry and texture in ammonia retention at ambient conditions, Adv. Funct. Mater. 20 (10) (2010) 1670–1679.
[45] Y. Su, X. Rong, A. Gao, Y. Liu, J. Li, M. Mao, X. Qi, G. Chai, Q. Zhang, L. Suo, Rational design of a topological polymeric solid electrolyte for high-performance all-solid-state alkali metal batteries, Nat. Commun. 13 (1) (2022) 4181.
[46] J. Hu, C. Lai, K. Chen, Q. Wu, Y. Gu, C. Wu, C. Li, Dual fluorination of polymer electrolyte and conversion-type cathode for high-capacity all-solid-state lithium metal batteries, Nat. Commun. 13 (1) (2022) 7914.
[47] H. Lee, H. Nam, J.H. Moon, Seamless integration of nanoscale crystalline-amorphous MoO3 domains for high-performance lithium-sulfur batteries, Energy Storage Mater. 70 (2024) 103551.
[48] Y.-S. Su, Y. Fu, T. Cochell, A. Manthiram, A strategic approach to recharging lithium-sulphur batteries for long cycle life, Nat. Commun. 4 (1) (2013) 2985.
[49] K. Oh, H. Nam, Y.J. Chung, J.H. Moon, Dry carbothermal reaction-enabled ultra-dense nanoparticle coatings for high-performance Li-S batteries, Chem. Eng. J. 499 (2024) 156229.
[50] S. Abbrent, J. Plestil, D. Hlavata, J. Lindgren, J. Tegenfeldt, Å. Wendsjö, Crystallinity and morphology of PVdF–HFP-based gel electrolytes, Polymer 42 (4) (2001) 1407–1416.
[51] J. Gou, K. Cui, S. Wang, Z. Zhang, J. Huang, H. Wang, An anisotropic strategy for developing polymer electrolytes endowing lithium metal batteries with electrochemo-mechanically stable interface, Nat. Commun. 16 (1) (2025) 3626.
[52] Y. He, C. Wang, R. Zhang, P. Zou, Z. Chen, S.-M. Bak, S.E. Trask, Y. Du, R. Lin, E. Hu, A self-healing plastic ceramic electrolyte by an aprotic dynamic polymer network for lithium metal batteries, Nat. Commun. 15 (1) (2024) 10015.
[53] Z. Li, R. Yu, S. Weng, Q. Zhang, X. Wang, X. Guo, Tailoring polymer electrolyte ionic conductivity for production of low-temperature operating quasi-all-solid-state lithium metal batteries, Nat. Commun. 14 (1) (2023) 482.
[54] X. Liang, D. Han, Y. Wang, L. Lan, J. Mao, Preparation and performance study of a PVDF–LATP ceramic composite polymer electrolyte membrane for solid-state batteries, RSC Adv. 8 (71) (2018) 40498–40504.
[55] S. Yeom, H. Jo, H. Lee, J.H. Moon, Lithiating cathodes for Li-S batteries: Regulating Li2S electrodeposition to enhance sulfur utilization, Energy Storage Mater. 71 (2024) 103644.

[56] M. Hahn, S. Schindler, L.-C. Triebs, M.A. Danzer, Optimized process parameters for a reproducible distribution of relaxation times analysis of electrochemical systems, Batteries 5 (2) (2019) 43.

[57] Z. Yao, T. Fu, T. Pan, C. Luo, M. Pang, S. Xiong, Q. Guo, Y. Li, S. Liu, C. Zheng, Dynamic doping and interphase stabilization for cobalt-free and high-voltage Lithium metal batteries, Nat. Commun. 16 (1) (2025) 2791.

[58] K. Um, C. Jung, H. Nam, H. Lee, S. Yeom, J.H. Moon, Janus architecture host electrode for mitigating lithium-ion polarization in high-energy-density Li–S full cells, Energy Environ. Sci. 17 (23) (2024) 9112–9121.

[59] J. Li, H. Zhang, Y. Cui, H. Da, H. Wu, Y. Cai, S. Zhang, Constructing robust cathode/Li interfaces and intensifying ion transport kinetics for PEO-based solid-state lithium-sulfur batteries, Chem. Eng. J. 454 (2023) 140385.

[60] J. Sheng, Q. Zhang, C. Sun, J. Wang, X. Zhong, B. Chen, C. Li, R. Gao, Z. Han, G. Zhou, Crosslinked nanofiber-reinforced solid-state electrolytes with polysulfide fixation effect towards high safety flexible lithium–sulfur batteries, Adv. Funct. Mater. 32 (40) (2022) 2203272.

[61] C. Yan, Y. Zhou, H. Cheng, R. Orenstein, P. Zhu, O. Yildiz, P. Bradford, J. Jur, N. Wu, M. Dirican, Interconnected cathode-electrolyte double-layer enabling continuous Li-ion conduction throughout solid-state Li-S battery, Energy Storage Mater. 44 (2022) 136–144.

[62] M. Wang, H. Su, Y. Zhong, X. Hu, X. Wang, C. Gu, J. Tu, Localized S-Li2s Conversion With Accelerated Kinetics Mediated by Mixed Conductive Shell for High-Performance Solid-State Lithium-Sulfur Battery, Adv. Energy Mater. 14 (9) (2024) 2302255.

[63] M. Li, Z. Huang, Y. Liang, Z. Wu, H. Zhang, H. Chen, S. Zhang, Accelerating lithium-ion transfer and sulfur conversion via electrolyte engineering for ultra-stable all-solid-state lithium–sulfur batteries, Adv. Funct. Mater. 35 (3) (2025) 2413580.

[64] Y. Xia, Y. Liang, D. Xie, X. Wang, S. Zhang, X. Xia, C. Gu, J. Tu, A poly (vinylidene fluoride-hexafluoropropylene) based three-dimensional network gel polymer electrolyte for solid-state lithium-sulfur batteries, Chem. Eng. J. 358 (2019) 1047–1053.

[65] F. Chen, P.G. Puente, Y. Zhang, S. Cao, X. Lu, Z. Yi, Q. Shen, J. Li, All-solid-state lithium-sulfur batteries assembled by composite polymer electrolyte and amorphous sulfur/rGO composite cathode, Solid State Ionics 380 (2022) 115926.

[66] H. Zhang, U. Oteo, X. Judez, G.G. Eshetu, M. Martinez-Ibanez, J. Carrasco, C. Li, M. Armand, Designer anion enabling solid-state lithium-sulfur batteries, Joule 3 (7) (2019) 1689–1702.

[67] Y. Liu, H. Liu, Y. Lin, Y. Zhao, H. Yuan, Y. Su, J. Zhang, S. Ren, H. Fan, Y. Zhang, Mechanistic investigation of polymer-based all-solid-state lithium/sulfur battery, Adv. Funct. Mater. 31 (41) (2021) 2104863.